

# The 1.87 and 2.07 Micron Observations of Three Galactic Center Clusters with miniTAO at Atacama: Classification of Stellar Components in Massive Star Clusters

Masuo Tanaka<sup>1\*</sup>, Shin-ichiro Okumura<sup>2</sup>, Hidenori Takahashi<sup>1</sup>, Kentaro Osawa<sup>1</sup>, Kentaro Motohara<sup>1</sup>, Masahiro Konishi<sup>1</sup>, Ken Tateuchi<sup>1</sup>, Natsuko Kato<sup>1</sup>, Tomoki Morokuma<sup>1</sup>, Ryou Ohsawa<sup>1</sup>, Shintaro Koshida<sup>1,3</sup>, Yuzuru Yoshii<sup>1,4</sup>, and Yuji Nishimura<sup>5</sup>

<sup>1</sup>*Institute of Astronomy, The University of Tokyo, 2-21-1 Osawa, Mitaka, Tokyo 181-0015, Japan*

<sup>2</sup>*Bisei Spaceguard Center, Japan Spaceguard Association, Okura, Bisei-cho, Ibara, Okayama, 714-1411, Japan*

<sup>3</sup>*Subaru Telescope, National Astronomical Observatory of Japan, 650 North Aohoku Place, Hilo, HI 96720, USA*

<sup>4</sup>*Steward Observatory, The University of Arizona, Tucson, AZ87512, USA*

<sup>5</sup>*Nishimura Co. Ltd., 10-3 Kamitobashirikiri-cho, Minami-ku, Kyoto, 601-8115, Japan*

Accepted; Received; in original form 2017 June 1

## ABSTRACT

In order to investigate evolution of massive stars in massive star clusters by a search for massive post-main-sequence stars together with massive young stellar objects, we have constructed a near-infrared image set: narrow-band images of 1.87 and 2.07  $\mu\text{m}$ , and  $K_S$  standard-band with miniTAO, a 1-m infrared telescope at Atacama. First of all we observed the well-known three massive star clusters near the Galactic center: the Galactic Center cluster, the Quintuplet cluster, and the Arches cluster. Color-color diagrams made from the set of the images show clear excesses in 1.87  $\mu\text{m}$  for WN-type Wolf-Rayet stars, Luminous Blue Variables, and Ofpe stars, and also clear excesses in 2.07  $\mu\text{m}$  for WC-type Wolf-Rayet stars. Most of the known Wolf-Rayet stars and Luminous Blue Variables in our observed area are detected and shown in these diagrams. Our detection in 1.87  $\mu\text{m}$  agrees well to the 1.87  $\mu\text{m}$  detection with *Hubble Space Telescope* by Dong et al.

The color-color diagrams enable us to find not only various types of the emission-line stars, but also extinction for each star to draw extinction maps. The 1.87  $\mu\text{m}$ -excess of WN stars seems to have a clear relation to the absolute  $K_S$  magnitude. The relation suggests that the 1.87  $\mu\text{m}$ -excess originates in recombination line emission of He II, and the absolute  $K_S$  magnitude includes free-free radiation. Furthermore, the absolute  $K_S$  magnitude of WN-Late stars, excluding the component of the free-free emission, seems to have nearly the common  $K_S$  magnitude. On the other hand, almost all Mira variables reported by Matsunaga et al. are detected in our images. By using the extinction maps, several tens of extremely red sources except for Mira variables are also detected. They are possibly considered to be low-temperature ( $T < 1000$  K) objects.

**Key words:** stars: massive star – stars: Wolf-Rayet – Galaxy: center – infrared: stars.

## 1 INTRODUCTION

Massive stars essentially affect the structure and evolution of galaxies through their huge radiative and mechanical energy

output and also their production of plentiful heavy elements during their very short lifetimes. In spite of the importances of the massive stars, we have not yet had enough knowledge of the birth and evolution of massive stars. For example, it is considered that massive stars have a tendency to be formed in clusters (e.g., Zwart et al. 2010), while many iso-

\* E-mail: mtanaka@ioa.s.u-tokyo.ac.jp

lated (that is, not belonging to clusters) massive stars have been discovered in the Galactic Center area (e.g., Dong et al. 2011; Mauerhan et al. 2010a,c). Moreover, it is uncertain whether the formation in a certain cluster can be instantaneous or not. It is considered that their huge radiative and mechanical energy may trigger subsequent generations of star formation (e.g., Davies et al. 2012). On the other hand, the evolution in their last stages has been expressed as Conti scenario (cf. Conti 1975; Crowther 2007) for various initial mass of massive stars, however recently, the evolution to supernovae of various types (type Ib/c and type IIP/L/n) is considered to depend on not only the initial mass, but also metallicity, rotation, single or binary, etc. (cf. Smartt 2009).

As likeliest candidates of the progenitors of type Ib/c supernovae, Wolf-Rayet stars have been searched for several decades. See the reviews by Crowther (2007, 2015), and also the catalogues by van der Hucht (2001, 2006) and the online catalogue by Crowther<sup>1</sup>. In particular, since 2000 many investigations have been carried out in infrared wavelengths (e.g., Homeier et al. 2003a,b; Shara et al. 2012, 2009; Mauerhan et al. 2011). Their methods are mainly imaging observations with narrow-band filters followed by spectroscopic observations. Recently, Davies et al. (2012) reported a massive star cluster beyond the Galactic Center detected in Pa $\alpha$  images with *Hubble Space Telescope*. In spite of such recent investigations, many massive star clusters are considered to be still hidden in regions with higher extinction in the Galaxy.

In order to search massive-star formation sites with higher extinction, through detections of not only evolved stages of the stars such as Wolf-Rayet stars (WR), Luminous Blue Variables (LBV), Red/Blue supergiants (RSG/BSG), Yellow Hypergiants (YHG), but also Massive Young Stellar Objects (MYSO) or pre-main-sequence stages, we have constructed a simple near-infrared narrow-band imaging system. We adopted a three-filter system which consists of two narrow-band filters in  $2\mu\text{m}$  range and  $K_S$  standard broad-band filter for detection of distinctive emission lines from massive stars. We also need to estimate extinction from our data set, especially for the search in regions with high extinction. Pa $\alpha$  ( $1.875\ \mu\text{m}$ ) and He II  $n=8-6$  ( $1.875\ \mu\text{m}$ ) and also 6-5 ( $1.864\ \mu\text{m}$ ) are intrinsically strong among H I and He II lines around  $2\mu\text{m}$ . They are, however, usually difficult to detect in ground-based observations due to strong terrestrial H<sub>2</sub>O absorption. We have constructed a 1-m infrared telescope, miniTAO (The University of Tokyo Atacama Observatory; Minezaki et al. 2010), at the summit of Cerro Chajnantor (altitude of 5640 m), Atacama, northern Chile in 2009 to make a seamless observations in near-infrared wavelengths from the ground (Tateuchi et al. 2015; Tanabé et al. 2013; Konishi et al. 2015; Tateuchi et al. 2012). This telescope makes us possible to carry out the observations in  $1.87\ \mu\text{m}$  range. Finally, we decided to make two narrow-band filters: one is  $1.87\ \mu\text{m}$  for H I and He II lines, the other is  $2.07\ \mu\text{m}$  for CIV line for the observations with miniTAO.

Since the Galactic Center region is the most dense area of massive stars in the Galaxy, and there are well-studied three famous clusters: the Galactic Center cluster, the Quintuplet cluster, and the Arches cluster, which have different ages and different classes of stars (e.g., Figer et al. 1999,

2002; Martins et al. 2007, 2008; Mauerhan et al. 2010c), we selected this area for the first search with our system. We expect to understand the possibility and problems/limitations of our method from the data. In this paper, we mainly describe our method and the detected sources phenomenologically. The observations and data reduction are described in Section 2 and our method in Section 3. The details of the detected sources are discussed in Section 4 and we summarize the results of the paper in Section 5.

## 2 OBSERVATIONS AND DATA REDUCTION

We have obtained  $5' \times 5'$  images centered on three massive-star clusters: the Galactic Center cluster, the Quintuplet cluster, and the Arches cluster, with two narrow-band filters of  $1.87$  and  $2.07\ \mu\text{m}$  and  $K_S$  filter. The observations were carried out on photometric nights in June 2009 and April 2011, by using an infrared camera, ANIR (Atacama Near-Infrared Camera; Motohara et al. 2008; Konishi et al. 2015) attached to a 1-m infrared telescope, miniTAO (Minezaki et al. 2010), constructed at the summit of Cerro Chajnantor (altitude of 5640 m) in Atacama desert near the ALMA site, northern Chile. ANIR has a pixel scale of  $0''.30/\text{pixel}$  and FOV of  $5'.1$  with a  $1024 \times 1024$  HAWAII array. An average natural seeing at the site of the telescope is excellent to be around  $0''.6$ , so that it has one of the best image quality among the telescopes without AO systems. Therefore, we can resolve most WR stars except for the center of the Galactic Center cluster. The filters we used have the center wavelength and FWHM of ( $1876\ \text{nm}$ ,  $8\ \text{nm}$ ), ( $2074\ \text{nm}$ ,  $40\ \text{nm}$ ), and ( $2150\ \text{nm}$ ,  $320\ \text{nm}$ ) for  $N1875$ ,  $N207$ , and  $K_S$  filters, respectively (cf. Konishi et al. 2015). It is noted that the FWHM of  $N1875$  may be somewhat too narrow for our purpose. Images in five or nine dithered positions are combined into a final image. The effective image size is a little smaller than  $5'.1$  due to the dithering ( $10''$ ) observations. The observations are summarized in Table 1.

The data were reduced with standard packages of IRAF<sup>2</sup>. Basic reduction of dark subtraction and flat fielding were applied to all object images. Then “sky” image created from “off field” images was subtracted. Offsets among the dithered images were calculated, and dithered images were combined to one with median filtering. The position of the stars on the combined image of each filter was matched by 2-D coordinate transformation using the *geotran* task in IRAF.

Point-spread-function (PSF) fitting photometry was performed on each image with the DAOPHOT package in IRAF. For the absolute calibration of  $K_S$  band, we adjusted our instrumental magnitudes to the 2MASS magnitudes, whereas absolute calibration is difficult for two narrow-band filter images. In order to derive the relative flux ratios of  $F_{N207}/F_{K_S}$  and  $F_{N1875}/F_{K_S}$ , flux calibration for each filter image was done as follows. We converted the PSF fitting magnitude of each source to the corresponding total flux (total number of counts in ADU), then compared it to the

<sup>1</sup> <http://pacrowther.staff.shef.ac.uk/WRcat/>

<sup>2</sup> IRAF package are distributed by the National Optical Astronomy Observatory, and operated by the Association of Universities for Research in Astronomy, Inc., under contract with the National Science Foundation

**Table 1.** Summary of the observations

Filter		Galactic Center	Quintuplet	Arches
$K_S$	observation date	2009/06/10UT	2009/06/12UT	2011/04/26UT
	integration time [sec]	$4.2 \times 9$ dither = 37.8	$4.2 \times 9$ dither = 37.8	$10 \times 5$ dither $\times$ 7 set = 350
N1875	observation date	2009/06/10UT	2009/06/11UT	2011/04/26UT
	integration time [sec]	$120 \times 8$ dither = 960	$120 \times 9$ dither = 1080	$36 \times 5$ dither $\times$ 4 set = 720
N207	observation date	2009/06/10UT	2009/06/12UT	2011/04/26UT
	integration time [sec]	$30 \times 9$ dither = 270	$20 \times 9$ dither = 180	$50 \times 5$ dither $\times$ 8 set = 2000

**Table 2.** Summary of the data

	Galactic Center	Quintuplet	Arches	
center of the image	RA(2000) (h:m:s)	17:45:39.73	17:46:13.63	17:45:49.98
	DEC(2000) ( $^{\circ}$ : $'$ : $''$ )	-29:00:21.8	-28:49:37.5	-28:49:55.6
effective image size	286'' $\times$ 286''			
number of stars with $K_S < 13$ mag	3605	1955	1621	
average of $F_{N207}/F_{K_S}$	0.1041	0.1097	0.1095	
average $A_{K_S}$ [mag] <sup>1)</sup>	3.15	2.40	2.43	
normalization factor for $F_{N207}/F_{K_S}$ <sup>2)</sup>	0.130	0.130	0.130	
average of $F_{N1875}/F_{K_S}$	0.00647	0.00667	0.00728	
Atmospheric Transmittance in N1875 <sup>3)</sup>	0.37	0.31	0.34	
PWV [mm] <sup>3)</sup>	0.7	0.9	0.8	
Airmass	1.26	1.16	1.06	
normalization factor for $F_{N1875}/F_{K_S}$ <sup>4)</sup>	0.0161	0.0134	0.0147	

1) See Section 3.2.

2) See Section 3.1.

3) See Section 3.3.

4) See Sections 3.1 and 3.3.

total flux derived from aperture photometry. They show a proportional relation when each source has no close neighbor. When neighbors are within the aperture radius, the total flux in aperture photometry becomes larger than that in PSF fitting photometry, whereas it tends to be smaller when neighbors are in the annular sky fitting region. The conversion coefficient was determined by using sources with no neighbor around. From the final converted flux of  $F_{K_S}$ ,  $F_{N207}$ , and  $F_{N1875}$ , we obtained the flux ratio of  $F_{N207}/F_{K_S}$  and  $F_{N1875}/F_{K_S}$  for all sources.

We decided to use the stars with  $K_S < 13$  mag for the following discussion. In this case, photometric errors are  $\sim 10\%$  at most. The data and some results are summarized in Table 2. The details of this table are described in Section 3.

### 3 METHOD

The wavelengths of these two narrow-band filters are selected for detection of strong and major emission lines from massive stars. The N207 includes C IV 3d<sup>2</sup>D-3p<sup>2</sup>P (2078 nm) emission line, which is expected in WC-type WR stars. It is noted that He I 2p<sup>1</sup>P-2s<sup>1</sup>S (2058 nm) may also contribute partially to N207. On the other hand, N1875 includes Pa $\alpha$  (1875 nm) and/or He II  $n=8-6$  (1875 nm, almost

the same wavelength as Pa $\alpha$ ),  $n=6-5$  (1864 nm) emission lines in LBVs, Ofpe stars, and WN-type WR stars. In particular, the latter He II  $n=6-5$  can contribute in N1875 if the stellar wind velocity of the WR exceeds  $\sim 1000$  km s<sup>-1</sup>.

One may usually prepare two filters: “on-line” and “off-line”, for the quantitative detection of emission lines, but here, we use  $K_S$  standard broad-band filter as the “off-line” one for saving the observation time. The  $K_S$  data can also be compared to archive data (i.e., 2MASS). It is noted that the wavelength range of N207 is within that of  $K_S$ .

In the following, we describe our filter system has good performances in not only detection of such emission-line stars, but also estimates of extinction similar to the standard  $JHK_S$  photometry. As a result of this, we expect to detect also MYSOs or the related sources in the set of our images.

#### 3.1 Normalization Factors of $F_{N207}/F_{K_S}$ and $F_{N1875}/F_{K_S}$ Ratios

We determine the “normalization factors” of  $F_{N207}/F_{K_S}$  and  $F_{N1875}/F_{K_S}$  ratios in our filter system as follows. By using the specifications of these filters, i.e., the wavelength dependence of the transmittance, the value of  $F_{N207}/F_{K_S}$  and

$F_{N1875}/F_{K_S}$  ratios are calculated to be 0.130 and 0.0432, respectively, for sources with  $\lambda^{-4}$  spectra (the Rayleigh-Jeans side of the Planck function). That is, after this normalization, these ratios equal to unity for the sources with  $\lambda^{-4}$  spectra and no extinction, and these data are plotted on the origin in the (logarithmic) color-color diagram (see Figs. 1, 2, 3).

We also simulated the ratios of  $F_{N207}/F_{K_S}$  for various kinds of massive stars: WRs including WC and WN-type, LBVs, YHGs, O-type stars of early to late subtypes, and Supergiants from B-type to M-type which we had made spectroscopic observations (Nishimaki et al. 2008; Yamamuro et al. 2007, ; non-published data). The results are as follows: for almost all stars, except for WC-type WRs, the  $F_{N207}/F_{K_S}$  ratio has a value of  $\sim 0.130$ , whereas WC-type (except for WC9 and WCLd) stars have much larger values of 0.2-0.4 due to strong C IV 3d<sup>2</sup>D-3p<sup>2</sup>P emission. The samples for the above simulations are corrected for extinctions. On the other hand, for the  $F_{N1875}/F_{K_S}$  ratios we cannot simulate them due to no spectral data around 1.87  $\mu\text{m}$ . In consequence, in the case of no-extinction, the normalization factors of  $F_{N207}/F_{K_S}$  and  $F_{N1875}/F_{K_S}$  of our system are adopted to be 0.130 and 0.0432 with errors of a few %.

### 3.2 Extinction from $F_{N207}/F_{K_S}$

In practice, the observed sources have a certain degree of extinction. We can approximately find the extinction for each source by comparing the observed  $F_{N207}/F_{K_S}$  ratio to the value of 0.130 described above, in the case that the sources have no distinct emission/absorption lines and follow  $\lambda^{-4}$  spectra in the 2  $\mu\text{m}$  range. We adopt the extinction law;  $A_\lambda \propto \lambda^{-2.0}$  by (Nishiyama et al. 2006, 2008, see these references for the detailed discussion). With the above normalization factor of 0.130, we derive

$$A_{K_S} = -\log(F_{N207}/F_{K_S}/0.130) \times 32.6. \quad (1)$$

Average extinction,  $A_{K_S}$ , for each image is derived by averaging  $F_{N207}/F_{K_S}$  of the detected stars in the image, except for the sources with large or small values in  $F_{N207}/F_{K_S}$  which are possibly emission-line sources (e.g., WC stars) or extremely red sources (see the discussion in Section 4.5). In the calculations, we restricted the data to  $K_S=10-12$  mag in order to exclude Miras/LPVs. The derived averages of  $F_{N207}/F_{K_S}$  and  $A_{K_S}$  are summarized in Table 2.

### 3.3 Atmospheric Transmittance in $N1875$ from $F_{N1875}/F_{K_S}$

In principle, we could estimate the extinction also from the data of  $F_{N1875}/F_{K_S}$  and this value of extinction would agree with that from  $F_{N207}/F_{K_S}$ . However, the atmospheric transmittance in  $N1875$  is low and unstable unlike the case of 2 $\mu\text{m}$  range even if the observations are carried out at the high altitude (5640 m). Therefore, the data of  $F_{N1875}/F_{K_S}$  can be used to estimate average atmospheric transmittances in  $N1875$  by using the values of  $A_{K_S}$  derived from  $F_{N207}/F_{K_S}$  above.

The average atmospheric transmittances in  $N1875$  for a variety of precipitable water vapor (PWV) are calculated (cf. ATRAN; Tateuchi et al. 2012) and show that the transmittance is very sensitive to both of wavelengths in  $N1875$  and

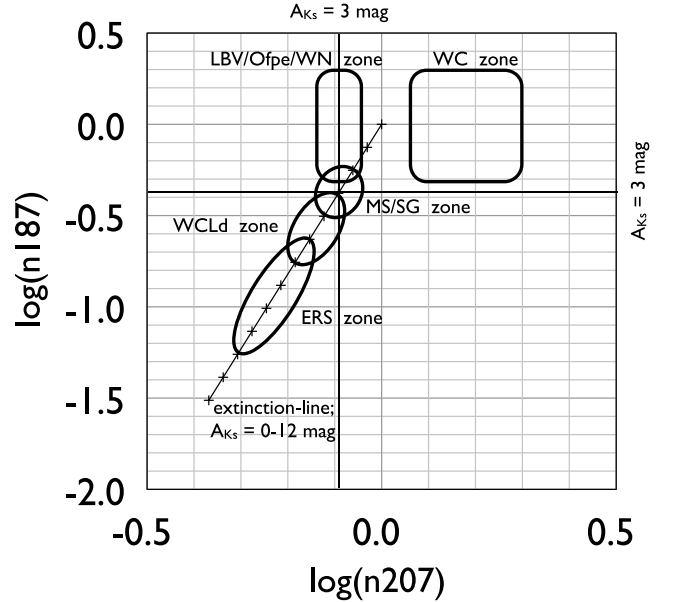


**Figure 1.** Zone of classification on  $\log(n207)$  vs.  $\log(n187)$  diagram for the case of Galactic Center areas with average  $A_{K_S} \sim 3$  mag. The extinction line is also drawn.

PWV. Therefore, the detection of “narrow” line with this filter must be sensitive to the radial velocity of the sources together with the PWV at the time of the observations. For example, this may be the case of Pa $\alpha$  of LBV.

On the other hand, the average atmospheric transmittance in  $N1875$  at the observations can be estimated by using stellar continuum light. That is, based on the extinction  $A_{K_S}$  estimated from  $F_{N207}/F_{K_S}$ , we can derive average atmospheric transmittances in  $N1875$  from the observed  $F_{N1875}/F_{K_S}$  ratios and the normalization factors of 0.0432 for the case of no atmospheric absorption derived in Section 3.1. The average  $F_{N1875}/F_{K_S}$  and the atmospheric transmittances derived from the average  $F_{N1875}/F_{K_S}$  are also summarized in Table 2. The derived average atmospheric transmittances range in 0.31-0.37, corresponding to PWV=0.9-0.7 mm in our observations. Anyway they are not the best values for the site. For example, in the other observation run for LMC (Takahashi et al., in preparation) we have the average atmospheric transmittance of  $\sim 0.5$ , corresponding to PWV=0.35 mm (cf. Konishi et al. 2015).

Finally, the normalization factors of  $F_{N1875}/F_{K_S}$  which are corrected for the atmospheric transmittances in each image are also calculated and listed in Table 2. In the calculations, we also used the data with  $K_S=10-12$  mag (cf. Section 3.2) and removed the sources with large or small values in  $F_{N1875}/F_{K_S}$  which are possibly emission-line sources (e.g., WN stars, LBVs, and emission stars) or extremely red sources. In the discussions below, we use the following notations as the normalized ratios of  $F_{N207}/F_{K_S}$  and  $F_{N1875}/F_{K_S}$ :

$$n207 \equiv F_{N207}/F_{K_S}/0.130, \quad (2)$$

$$n187 \equiv F_{N1875}/F_{K_S}/(\text{normalization factor for each cluster}). \quad (3)$$

These notations are independent of the atmospheric trans-

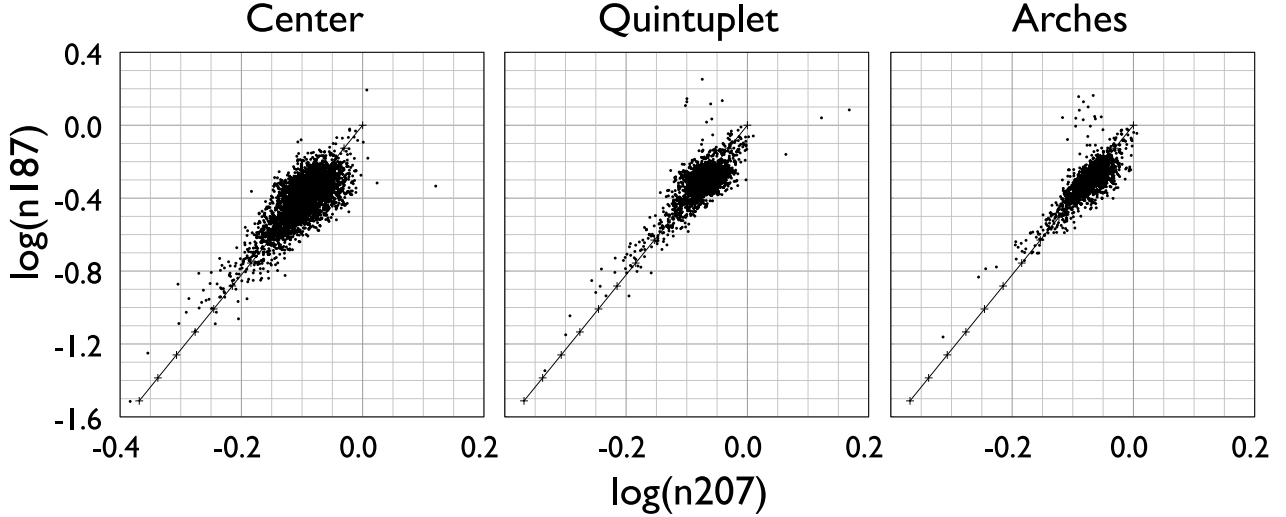


**Figure 2.** Data plot of the sources with  $K_S < 13$  mag in the three cluster areas on the  $\log(n207)$  vs.  $\log(n187)$  diagram. The data plotted on this figure have the S/N ratios  $\gtrsim 8$ , and error bars are omitted for easy-looking of the distribution of very large data points. The extinction line ( $A_{K_S} = 0$  to 12 mag from the origin to bottom-left) is also drawn.

mittances, so that it is convenient for us to compare the data on different observational conditions.

### 3.4 Zones for Various Kinds of Sources on the Color-Color Diagram: $\log(n207)$ vs. $\log(n187)$

Fig. 1 shows a color-color diagram of  $\log(n207)$  vs.  $\log(n187)$ . On this diagram we also draw an “extinction-line” with  $A_{K_S} = 0$  to 12 mag. This line satisfies the following relation:

$$\log(n187) = \log(n207) \times 4.10 \quad \text{for } \log(n207) < 0. \quad (4)$$

On the color-color diagram (Fig. 1), we set the following zones: LBV/Ofpe/WN zone (upper), WC zone (upper-right), Main Sequence/Supergiant zone (center), WCLd zone (center), and Extremely Red Sources (ERS; Miras and low-temperature sources; see Section 4.5) zone (lower-left). Fig. 1 is for our case of the Galactic center, that is,  $A_{K_S} \sim 3$  mag. These zonings are empirical and see the discussion below for the details. In particular, the range of  $n207$  for WC zone is adopted from our spectra of WC (WC4-WC8) stars which have the ratios  $\log(n207)$  of 0.2-0.4 in low extinction cases (Nishimaki et al. 2008).

## 4 RESULTS AND DISCUSSION

We plot our data of the three cluster areas on the  $\log(n207)$  vs.  $\log(n187)$  diagram in Fig. 2. In the Galactic Center region, the majority of the detected stars in near-infrared may be considered to be red-clump giants with the peak of  $K_S \sim 14$  mag (cf. Nishiyama et al. 2006). As described above, we limit the sources with  $K_S < 13$  mag in the discussion so that the majority of the red-clump giants are probably not included in our data. In this figure, the majority of the observed stars are located along the extinction line around  $A_{K_S} = 2 \sim 4$  mag. These are considered to be massive main-sequence stars, BSGs/RSGs and bright red giants. We will describe our data in detail on the basis of

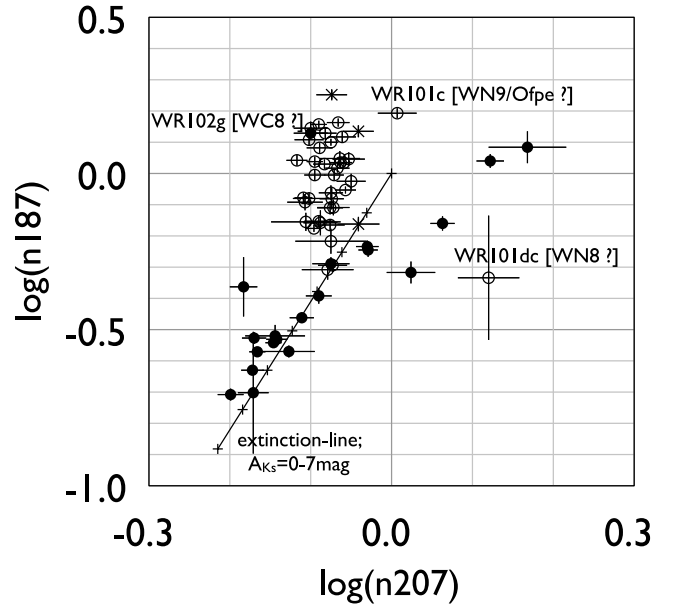


**Figure 3.** The known WR stars (17, 21, and 19 WRs of the Galactic Center, the Quintuplet, the Arches cluster area, respectively) plotted on the  $\log(n207)$  vs.  $\log(n187)$  diagram. Open and filled circles denote WN stars and WC (including WN/WC) stars, respectively. Three LBVs in Quintuplet area are added with asterisks. The extinction line is also drawn.

these diagrams in the following sections, especially focusing on the stars with excess in  $n207$  and/or  $n187$ , or extremely red colors.

### 4.1 Known WR Stars and LBVs on the Color-Color Diagram

First we confirm the known WR stars and LBVs on our color-color diagram. In the three clusters areas of  $5'$  square,

**Table 3.** Our detection of known WRs in the Galactic Center cluster area

ID	RA(2000)	DEC(2000)	$K_S$ [mag]	$\log(n187)^{1)}$	$\log(n207)^{1)}$	designation <sup>2)</sup>	type <sup>2)</sup>	$K$ [mag] <sup>2)</sup>	comment
C3294	17:45:40.26	-29:00:27.4	8.96	-0.176	-0.096	WR101nd	WN9/Ofpe	9.00	
C3288	17:45:40.45	-29:00:27.7	8.97	-0.702	-0.171	WR101oe	WCLd(Be?)	8.81	
C3216	17:45:39.80	-29:00:30.0	9.23	-0.080	-0.102	WR101e	WN8(WN8+WC9)	10.78(9.10)	
C3236	17:45:40.14	-29:00:29.4	9.46	-0.155	-0.106	WR101k	WN9/Ofpe	9.6	
C3282	17:45:40.13	-29:00:27.8	9.92	-0.165	-0.076	WR101l	WN9/Ofpe	9.83	
C3289	17:45:39.65	-29:00:27.5	9.93	-0.527	-0.170	WR101d	WC9(WN9/Ofpe?)	9.80	
C3296	17:45:39.92	-29:00:27.2	9.95	-0.570	-0.127	WR101g	WC9	9.96	
C3408	17:45:40.54	-29:00:23.3	10.07	-0.363	-0.183	WR101og	WCLd	10.27	
C3295	17:45:40.05	-29:00:27.2	10.08	-0.294	-0.073	WR101j	WN9/Ofpe	10.03	
C3174	17:45:40.09	-29:00:31.5	10.12	-0.092	-0.107	WR101ja	WN9/Ofpe	9.86	
C3056	17:45:39.55	-29:00:35.4	10.60	+0.193	+0.007	WR101c	WN9/Ofpe	10.70	WN/WC <sup>3)</sup>
C3096	17:45:39.37	-29:00:34.2	10.73	-0.289	-0.075	WR101a	WC8-9	10.40	
C5451	17:45:50.62	-28:59:19.6	10.82	-0.153	-0.090	Mauerhan-H	WN7	10.85	WR102b
C3304	17:45:39.73	-29:00:26.7	11.20	-0.308	-0.079	WR101db	WN9/Ofpe	11.60	
C3550	17:45:39.92	-29:00:18.5	11.53	-0.317	+0.024	WR101h	WN8/WC9	10.39	
C3181	17:45:39.30	-29:00:31.0	12.19	-0.217	-0.075	WR100a	WN7	12.71	
C3398	17:45:39.75	-29:00:23.5	12.37	-0.334	+0.120	WR101dc	WN8	12.0	WC <sup>3)</sup>

<sup>1)</sup>  $\log(n187) \equiv \log(F_{N1875}/F_{K_S}/0.0161)$  and  $\log(n207) \equiv \log(F_{N207}/F_{K_S}/0.130)$ , see Fig. 3 for the error of each star.

<sup>2)</sup> van der Hucht (2006); Mauerhan et al. (2010a); SIMBAD

<sup>3)</sup> See text

**Table 4.** Our detection of known WRs/LBVs in the Quintuplet cluster area

ID	RA(2000)	DEC(2000)	$K_S$ [mag]	$\log(n187)^{1)}$	$\log(n207)^{1)}$	designation <sup>2)</sup>	type <sup>2)</sup>	$K$ [mag] <sup>2)</sup>	comment
Q3526	17:46:14.72	-28:49:41.0	6.43	-0.520	-0.144	WR102dc	WC9d	6.57	
Q4405	17:46:17.99	-28:49:03.6	6.85	-0.162	-0.041	qF362	LBV	7.09	
Q2944	17:46:15.25	-28:50:03.7	6.95	+0.135	-0.041	Pistol Star	LBV	7.29	
Q873	17:46:05.64	-28:51:32.0	7.13	+0.252	-0.074	G0.120-0.048	LBV	7.46	
Q3410	17:46:15.88	-28:49:45.8	7.28	-0.571	-0.166	WR102ha	WC8-9d	7.24	
Q3707	17:46:14.81	-28:49:34.6	7.85	-0.531	-0.142	WR102dd	WC9d	7.82	
Q2695	17:46:17.42	-28:50:14.2	7.98	-0.542	-0.146	Mauerhan-K	WC9d	7.84	LPVS (V4649 Sgr)?
Q3632	17:46:14.15	-28:49:37.0	8.01	-0.630	-0.172	WR102da	WC9d	7.69	
Q3628	17:46:15.13	-28:49:37.3	8.81	+0.034	-0.059	WR102ea	WN9	9.17	
Q3784	17:46:14.34	-28:49:31.7	9.13	-0.708	-0.199	WR102db	WC9d	9.16	
Q3698	17:46:15.42	-28:49:34.8	9.23	-0.462	-0.111	LHO79	WC9d	9.55	
Q3609	17:46:15.96	-28:49:38.0	9.35	-0.053	-0.057	WR102hb	WN9	8.92	
Q3786	17:46:16.56	-28:49:31.9	10.17	+0.017	-0.067	WR102i	WN9	10.22	
Q3855	17:46:17.55	-28:49:29.1	10.25	-0.081	-0.074	WR102k	WN9	10.23	
Q3658	17:46:14.16	-28:49:35.5	10.42	-0.245	-0.029	LHO76	WC9d	10.54	
Q4115	17:46:14.07	-28:49:16.7	10.46	+0.117	-0.061	WR102d	WN9	10.5	
Q3920	17:46:13.06	-28:49:25.3	10.55	-0.234	-0.030	WR102ca	WC8-9	10.5	
Q3031	17:46:14.83	-28:50:00.6	10.55	-0.392	-0.090	WR102e	WC8	10.43	
Q2589	17:46:15.58	-28:50:18.3	11.28	-0.160	+0.063	WR102h	WC9	11.2	
Q3508	17:46:15.19	-28:49:41.9	11.36	+0.129	-0.100	WR102g	WC8	11.40	WNE <sup>3)</sup>
Q4086	17:46:17.52	-28:49:18.8	11.40	+0.040	+0.122	WR102j	WC<8	11.4	
Q3560	17:46:15.15	-28:49:40.0	11.40	+0.084	+0.168	WR102f	WC8	10.4	
Q5524	17:46:23.85	-28:48:11.1	11.47	+0.145	-0.100	Mauerhan-17	WN5b	11.43	
Q4330	17:46:11.15	-28:49:06.3	11.59	+0.108	-0.102	WR102c	WN6	11.6	

<sup>1)</sup>  $\log(n187) \equiv \log(F_{N1875}/F_{K_S}/0.0134)$  and  $\log(n207) \equiv \log(F_{N207}/F_{K_S}/0.130)$ , see Fig. 3 for the error of each star.

<sup>2)</sup> van der Hucht (2006); Mauerhan et al. (2010a); Mauerhan et al. (2010c); Liermann et al. (2009); Mauerhan et al. (2010b); SIMBAD

<sup>3)</sup> See text

several tens of WR stars and three LBVs (in the Quintuplet cluster area) have been discovered and summarized by van der Hucht (2006); Mauerhan et al. (2010a); Mauerhan et al. (2010c); Liermann et al. (2009); Mauerhan et al. (2010b). In Tables 3-5 we summarize the stars detected by us together with the previous data. In Fig. 3 we plot the WR stars and

LBVs detected in the three filters on the color-color diagram. The position of each star on the diagram is crucial for our method to classify the massive stars, therefore we describe all stars on the figures individually in the followings.

**Table 5.** Our detection of known WRs in the Arches cluster area

ID	RA(2000)	DEC(2000)	$K_S$ [mag]	$\log(n187)^{1)}$	$\log(n207)^{1)}$	designation <sup>2)</sup>	type <sup>2)</sup>	$K$ [mag] <sup>2)</sup>	comment
A2738	17:45:50.42	-28:49:22.2	9.86	+0.100	-0.075	WR102ah	WN8-9h	9.87	
A2677	17:45:50.46	-28:49:19.5	9.89	+0.035	-0.063	WR102aj	WN8-9h	9.56	
A2627	17:45:50.56	-28:49:17.5	10.16	+0.163	-0.066	WR102al	WN7-8	10.1	
A2840	17:45:50.82	-28:49:26.3	10.19	+0.157	-0.090	WR102bb	WN8-9	10.1	
A2740	17:45:50.20	-28:49:22.1	10.22	+0.030	-0.083	WR102ad	WN8-9	10.1	
A2718	17:45:50.39	-28:49:21.1	10.27	+0.082	-0.089	WR102ag	WN8-9	10.1	
A2497	17:45:50.25	-28:49:11.6	10.47	-0.005	-0.071	WR102ae	WN9h	10.47	
A2986	17:45:50.45	-28:49:31.9	10.55	+0.038	-0.095	WR102ai	WN8-9	10.6	
A2622	17:45:50.27	-28:49:17.1	10.56	+0.048	-0.064	WR102af	WN7-8	9.60/10.6	
A2833	17:45:49.69	-28:49:25.7	10.69	-0.078	-0.109	WR102aa	WN8-9	12.16/10.8	
A5615	17:45:55.37	-28:51:26.4	10.79	+0.129	-0.082	Mauerhan-I	WN5-6b	10.84	
A2742	17:45:50.67	-28:49:22.4	10.91	+0.046	-0.053	WR102ba	WN8-9	10.8	
A3755	17:45:48.55	-28:50:05.9	10.95	+0.042	-0.117	WR102a	WN8	11.0	
A2856	17:45:50.06	-28:49:26.4	10.99	-0.109	-0.072	WR102ab	WN7(O4-6If)	11.0	
A3091	17:45:53.38	-28:49:37.2	11.00	-0.062	-0.075	Mauerhan-12	WN8-9h	11.00	
A2696	17:45:50.51	-28:49:20.6	11.06	-0.025	-0.050	WR102ak	WN8-9	10.9	
A3246	17:45:48.58	-28:49:42.5	11.11	-0.110	-0.076	Mauerhan-11	WN8-9h	11.14	
A2817	17:45:51.46	-28:49:25.6	11.21	-0.005	-0.095	WR102bc	WN8	11.2	
A2868	17:45:50.12	-28:49:27.0	11.67	-0.158	-0.088	WR102ac	WN7	12.15/11.6	

<sup>1)</sup>  $\log(n187) \equiv \log(F_{N1875}/F_{K_S}/0.0147)$  and  $\log(n207) \equiv \log(F_{N207}/F_{K_S}/0.130)$ , see Fig. 3 for the error of each star.

<sup>2)</sup> van der Hucht (2006); Mauerhan et al. (2010a); Mauerhan et al. (2010c); Dong et al. (2011); SIMBAD

#### 4.1.1 The Galactic Center Cluster Area

In this cluster area, van der Hucht (2006) summarized 42 WR stars and one WR star was discovered by Mauerhan et al. (2010a). Among the 43 WR stars, we confirmed 17 stars in all three filters (Table 3). We also confirmed 11 stars with only  $K_S$  and  $N207$  and cannot derive the certain  $F_{N1875}$  fluxes of the 11 stars: WR101m, na, o, fa, b, i, oc, of, dd, f, and nc, because of strong Paschen  $\alpha$  nebosity in the area. Among non-identified 15 stars, 5 stars: WR101de, df, dh, di, and ea are located very close ( $< 1''$ ) to WR101e (C3216) so that we cannot resolve with our spatial resolution. In other words, our  $K_S$  magnitude of WR101e may include these 5 stars, where WR101e is the brightest among 6 stars. Among the residual 10 stars, WR101ma is very close to a very bright star GC IRS7 (M2I) and merges into it in our image; WR101n, oa, ob are detected in only  $K_S$ ; and others are not detected even in  $K_S$  with  $K_S < 13$  mag. Finally, we plot 17 stars in the Galactic Center cluster area on Fig. 3.

We now describe the positions of the 17 stars on the diagram one by one. Among 11 WN stars, four stars of C3294, C3236, C3282, C3174 are classified as WN9/Ofpe and located in LBV/Ofpe/WN zone with  $n187$ -excess, which means the location above the “extinction-line” with  $n207$  corresponding to  $A_{K_S} \sim 3$  mag. Other two stars C3295 and C3304 are also identified as WN9/Ofpe, but show no  $n187$ -excess. Stars C3295 and C3304 are located very near the center of the cluster so that  $N1875$  photometry seems to be difficult and the errors of  $\log(n187)$  may be larger than other sources in Fig. 3. Moreover, another WN9/Ofpe star, C3056 (=WR101dc) show a clear  $n207$ -excess together with a large  $n187$ -excess (Fig. 3 and Table 3); this star is possibly a WN/WC star (in transition) or WN+WC. Next three stars of C3216, C5451, C3181 which are classified as WN7-8 also located in LBV/Ofpe/WN zone. As described above, C3216 may be multiple of WR stars in our data. Finally,

C3398 (=WR101dc), which is classified as WN8 in van der Hucht (2006) shows no excess in  $n187$  and a clear excess in  $n207$ , and the  $K_S$  magnitude is consistent with van der Hucht (2006), so that it is possibly a WC star.

On the other hand, among six WC stars (including one WN/WC), C3550, which is identified as WN8/WC9, shows  $n207$ -excess. Three stars C3288, C3289, C3296 are classified as WCLd/WC9 and located in WCLd zone, which are along the “extinction-line” with  $A_{K_S} = 3-6$  mag (see Section 3.4). C3096 (WC8-9) is also on the extinction-line, but does not show large extinction. Finally, C3408 (WCLd) is located above the extinction line although the error of  $F_{N1875}$  flux is large. Although C3408 is classified as WCLd in van der Hucht (2006), it has too large  $n187$ . This star seems to be isolated and is bright enough;  $K_S$  magnitude is consistent between our data and that of van der Hucht (2006). Considering a star C3406, which is located near C3408, has also uncertainly large  $n187$ , we suppose the inconsistency might be due to the large uncertainty of  $n187$ . It is noted that Dong et al. (2011) do not detect  $F_{N1875}$  excess for these stars. We suppose  $F_{N1875}$  is affected by strong Pa $\alpha$  nebosity in the central area.

As described here, for the stars very close to the Galactic Center, our photometric results (especially  $F_{N1875}$ ) are somewhat uncertain because of the very high stellar density and strong diffuse emission of Pa $\alpha$ . Therefore our classification for such stars based on our data is partially uncertain. However, this uncertainty is mainly due to the very high stellar density of this unique area for the observations by using a 1m-telescope without AO system, not due to our methodology.

#### 4.1.2 The Quintuplet Cluster Area

In this cluster area, there are 17 WR stars summarized by van der Hucht (2006) and other 4 WR stars discovered by

**Table 6.** Correspondence of  $F_{N1875}$ -detection to Dong et al. (2011) for the sources of the Galactic Center cluster area

Dong et al. (2011)				This study				
ID	$K_S$ [mag]	$r \equiv f187/f190$	Type	ID	$K_S$ [mag]	$\log(n187)^*$	$\log(n207)^*$	comment
P38	8.9	1.1	O4-7I	C1483	8.89	-0.102	-0.044	small 187-excess
P109	10.9	1.9	WN7	C5451	10.82	-0.153	-0.090	Table3
P117	10.3	2.9	WN9/Ofpe	C3056	10.60	+0.193	+0.007	Table3
P119		2.0	WN7	C3181	12.19	-0.217	-0.075	Table3
P120		1.8	WC8/9	C3096	10.73	-0.289	-0.075	Table3
P121		1.2	WN9/Ofpe	C3294	8.96	-0.176	-0.096	Table3
P122	9.1	1.6	WN8+WC9	C3216	9.23	-0.080	-0.102	Table3
P123		2.0	WN9/Ofpe	C3605	10.05		-0.181	
P124	11.5	1.7	WN8/WC9	C3550	11.53	-0.317	+0.024	Table3
P125		1.3	WN9/Ofpe	C3304	11.20	-0.308	-0.079	Table3
P126	12.0	1.5	WN8	C3398	12.37	-0.334	+0.120	Table3
P129		1.2	WN9/Ofpe	C3282	9.92	-0.165	-0.076	Table3
P130		2.4	WN5/6	C3245	11.02		-0.144	
P131		1.8	WC9	C3301	10.13	-0.531	-0.154	small 187-excess
P132	11.1	1.9	WN8	C3111	11.58		-0.051	
S12		1.1		C5579	12.56	-0.684	-0.120	no 187-excess
S15		2.1		C3405	11.23	-0.337	-0.096	small 187-excess
S37		1.3		C4913	10.50	-0.474	-0.121	no 187-excess
S39		1.2		C4877	10.19	-0.350	-0.105	small 187-excess
S80		1.2		C4174	13.13	-0.261	-0.084	small 187-excess
S88	11.3	1.0		C136	11.37	-0.224	-0.043	no 187-excess
S89	9.7	1.0		C1464	9.42	-0.130	-0.032	no 187-excess
S90		1.2		C1366	11.76		-0.195	
S91	14.0	1.1		C495	13.43	-0.225	-0.064	small 187-excess
S92	8.3	1.0		C552	8.33	-0.083	-0.008	no 187-excess
S164	9.6	1.1	WN9/Ofpe	C3295	10.08	-0.294	-0.073	Table3
S165	7.0	1.2	WN9/Ofpe	C3236	9.46	-0.155	-0.106	Table3
S167		1.1		C1171	12.68	-0.489	-0.134	small 187-excess
				C3174	10.12	-0.092	-0.107	Table3

\*  $\log(n187) \equiv \log(F_{N1875}/F_{K_S}/0.0161)$  and  $\log(n207) \equiv \log(F_{N207}/F_{K_S}/0.130)$

We cannot identify 12 sources in Dong's list: P110, P118, P127, P128, P133, S13, S81, S82, S87, S93, S94, S166, (S162=P129?, S163=P117?)

Mauerhan et al. (2010a); Mauerhan et al. (2010c); Liermann et al. (2009). We confirmed all of the 21 stars (Table 4) and plot them on Fig. 3. Seven stars Q3628, Q3609, Q3786, Q3855, Q4115, Q5524, Q4330 are classified as WN stars (Table 4) and located in LBV/Ofpe/WN zone with  $n187$ -excess, which means the location above the “extinction-line” with  $n207$  corresponding to  $A_{K_S} \sim 2$ -3 mag.

On the other hand, seven stars Q3526, Q3410, Q3707, Q2695, Q3632, Q3784, Q3698 classified as WC9d and are located in WCLd zone, which are along the “extinction-line” with  $A_{K_S}=3$ -6 mag (see Section 3.4). According to SIMBAD, Q2695 may be a long period variable star (LPVS; V4649 Sgr). The location in the color-color diagram (Fig. 3) is also reasonable for LPVS. Other three stars Q3658(WC9d), Q3920(WC8-9), and Q3031(WC8) are on the extinction-line but do not show large extinction as the above seven stars. Moreover, three stars Q2589(WC9), Q4086(WC<8), and Q3560(WC8) are located in WC zone. Finally, Q3508 (=WR102g) classified as WC8 is located in the central area but seems to be isolated. Based on the location in our diagram, it is probably a WN star. This star is identified as LHO34 by Liermann et al. (2009), and their spectrum seems to indicate a feature of a WNE star. The  $f187$  result by Dong et al. (2011) shows also large

excess in  $f187/f190$  (see Section 4.2). Consequently, our classifications from the diagram of almost all sources in this area (except for Q3508) are consistent with previous ones. Furthermore, the  $K_S$  magnitude of our measurements are fairly consistent with those of the literature (except for Q3560=LHO47; see Table 4) in this area.

In Quintuplet area, three LBVs has been identified, which are qF362 (Q4405), the Pistol Star (Q2944), and G0.120-0.048 (Q873) (cf. Mauerhan et al. 2010b). The latter two stars show large excess in  $n187$ , but Q4405 has no  $n187$ -excess on the extinction-line with  $A_{K_S}=1.4$  mag, that is, the normal-star zone on our diagram. As described above, for LBVs Pa $\alpha$  may be the major contributor to  $f_{N1875}$ . The line width of Pa $\alpha$  in LBVs must be narrower, then the  $n187$  value can be affected largely due to the complicated atmospheric window in  $N1875$ . However, the non-detection (non-excess) of  $f187$  by Dong et al. (2011) should indicate that our non-excess of  $n187$  is not due to the atmospheric condition nor the radial velocity of qF362. The reason of non-excess of  $n187$  in qF362 may remain as a puzzle.

**Table 7.** Correspondence of  $F_{N1875}$ -detection to Dong et al. (2011) for the sources of the Quintuplet cluster area

Dong et al. (2011)				This study				
ID	$K_S$ [mag]	$r \equiv f187/f190$	Type	ID	$K_S$ [mag]	$\log(n187)^*$	$\log(n207)^*$	comment
P2	11.4	2.6	WN5b	Q5524	11.47	+0.145	-0.100	Table4
P3	12.3	1.1		Q6610	12.29	-0.281	-0.045	no 187-excess
P4	9.8	1.2	OBI	Q4491	9.80	-0.105	-0.076	clear 187-excess
P5	12.2	1.1		Q4204	12.75	-0.214	-0.107	small 187-excess
P6	10.4	1.5	WN9	Q3628	8.81	+0.034	-0.059	Table4
P7	8.9	1.5	WN9	Q3609	9.35	-0.053	-0.057	Table4
P8	9.8	1.2	O6-8If	Q3836	9.54	-0.138	-0.047	small 187-excess
P9	10.6	1.1	O6-8Ife	Q3766	9.53	-0.139	-0.052	small 187-excess
P10	9.9	1.1	O6-8Ifq	Q3690	9.82	-0.165	-0.020	no 187-excess
P11	10.2	1.5	WN9	Q3786	10.17	+0.017	-0.067	Table4
P12	11.3	2.7	WC8	Q3508	11.36	+0.129	-0.100	Table4
P13		2.2	WC8	Q3560	11.40	+0.084	+0.168	Table4
P15	11.7	1.1		Q4462	11.70	-0.209	-0.075	small 187-excess
P59	10.2	1.4	WN9	Q3855	10.25	-0.081	-0.074	Table4
P60	11.4	2.2	WC8	Q4086	11.40	+0.040	+0.122	Table4
P62	10.5	2.2	WN9	Q4115	10.46	+0.117	-0.061	Table4
P63	10.5	1.4	WC8-9	Q3920	10.55	-0.234	-0.030	Table4
P64	11.6	2.6	WN6	Q4330	11.59	+0.108	-0.102	Table4
P65	10.9	1.1		Q4656	10.91	-0.140	-0.080	clear 187-excess
P66	11.2	2.0	WC9	Q2589	11.28	-0.160	+0.063	Table4
P68	7.3	1.2	LBV	Q2944	6.95	+0.135	-0.041	Table4
P69	9.2	1.1	O6-8If?	Q4044	9.12	-0.178	-0.065	small 187-excess
P70	10.2	1.1	O3-8Ife	Q3264	10.34	-0.136	-0.073	clear 187-excess
P71	10.3	1.4	WC9d	Q3658	10.42	-0.245	-0.029	Table4
P72	10.5	1.1	O7-B0I	Q4011	10.51	-0.187	-0.087	small 187-excess
P73	10.5	1.2	WC8	Q3031	10.55	-0.392	-0.090	Table4
P75	10.5	1.3	O6If+	Q934	10.52	-0.132	-0.054	small 187-excess
P92	7.5	1.3	LBV	Q873	7.13	+0.252	-0.074	Table4
S2		1.6		Q1686	13.96	-0.291	-0.051	no 187-excess
S26		1.2		Q5043	6.60	-0.270	-0.054	no 187-excess
S30		1.5		Q2313	13.72	-0.240	-0.053	no 187-excess
S131	11.1	1.1		Q3337	11.16	-0.166	-0.064	small 187-excess

\*  $\log(n187) \equiv \log(F_{N1875}/F_{K_S}/0.0134)$  and  $\log(n207) \equiv \log(F_{N207}/F_{K_S}/0.130)$

We cannot identify 15 sources in Dong's list: P14, P67, P74, S1, S25, S27, S54, S56, S57, S58, S63, S64, S65, S129, S130

#### 4.1.3 The Arches Cluster Area

In this cluster area, there are 16 WR stars summarized by van der Hucht (2006) and other 3 WR stars discovered by Mauerhan et al. (2010a); Mauerhan et al. (2010c). All of these 19 stars are WN-type and we confirmed all stars. All stars show  $n187$ -excess on the diagram (Fig. 3). Furthermore, the  $K_S$  magnitude of our measurements are fairly consistent with the literature (see Table 5) in this area.

#### 4.2 Comparison with $f187/f190$ by Dong et al. (2011)

Dong et al. (2011) show a fine 1.87  $\mu\text{m}$  image observed with *Hubble Space Telescope*. They detected  $\sim 57,000$  sources in  $39' \times 15'$  (a net area of 416  $\text{arcmin}^2$ ) and listed 152 primary plus 189 secondary sources in their tables. Our three observed areas ( $5' \times 5'$  each) are covered by their observed region. Then, we can compare the detected sources. The results are summarized in Tables 6-8 for each area. For example, among the 34 sources detected by them in Arches area of  $5' \times 5'$ , we detected 26 sources (Table 8) and we cannot

find the residual 8 sources (one primary source is included). All of the known WR stars in the Arches cluster area are included in the both lists. Also in the other two areas, we have a similar results (Tables 6,7). They list 12 undetected known massive emission-line stars in their table 6. The all stars are included in van der Hucht (2006), and among them we detected two stars (C3174 and C3296) with our three filters. The star C3174 (WR101ja=E41; WN9/Ofpe) has  $n187$ -excess (see Tables 3 and 6), whereas C3296 (WR101g=E31; WC9) show no  $n187$ -excess as expected from the subtype (see Section 4.1 and Table 3).

We compare the “187-excess” between their  $r(=f187/f190) - 1$  and our excess  $\log(n187) \equiv \log(n187) - \log(n207) \times 4.10$  (eq. (6) below). Fairly good correlations between them are seen for Quintuplet and Arches areas. On the other hand, for the Galactic Center cluster area, we cannot see a good correlation as seen in the other two areas. We suppose that it is rather difficult to estimate the accurate  $f_{N1875}$  flux for each star due to the strong Pa $\alpha$  nebulosity in this area. The 187-excess of the three LBVs in Quintuplet

**Table 8.** Correspondence of  $F_{N1875}$ -detection to Dong et al. (2011) for the sources of the Arches cluster area

Dong et al. (2011)				This study				
ID	$K_S$ [mag]	$r \equiv f187/f190$	Type	ID	$K_S$ [mag]	$\log(n187)^*$	$\log(n207)^*$	comment
P17	10.6	2.0	WN8-9h	A2986	10.55	+0.038	-0.095	Table5
P18	10.8	1.7	WN8-9h	A2833	10.69	-0.078	-0.109	Table5
P19	11.1	1.9	WN8-9h	A3246	11.11	-0.110	-0.076	Table5
P20	11.0	1.2	O4-6If	A2856	10.99	-0.109	-0.072	Table5
P21	11.6	1.2		A2868	11.67	-0.158	-0.088	Table5
P22	11.0	1.3	WN8-9h	A3091	11.00	-0.062	-0.075	Table5
P25		1.2		A6980	12.92	-0.109	-0.083	clear 187-excess
P79	11.2	1.5	WN7	A2817	11.21	-0.005	-0.095	Table5
P80	9.9	2.0	WN8-9h	A2738	9.86	+0.100	-0.075	Table5
P81	10.1	2.1	WN7-8h	A2627	10.16	+0.163	-0.066	Table5
P82	10.1	2.1	WN8-9h	A2840	10.19	+0.157	-0.090	Table5
P83	12.0	1.8	WN8-9h	A2677	9.89	+0.035	-0.063	Table5
P84	10.1	2.0	WN8-8h	A2718	10.27	+0.082	-0.089	Table5
P85	10.1	1.7	WN8-9h	A2740	10.22	+0.030	-0.083	Table5
P86	10.5	1.5	WN8-9h	A2497	10.47	-0.005	-0.071	Table5
P87	9.6	1.8	WN7-8h	A2622	10.56	+0.048	-0.064	Table5
P88	10.8	1.6	WN8-9h	A2742	10.91	+0.046	-0.053	Table5
P89	10.8	1.2	O4-6If	A2604	10.75	-0.077	-0.039	small 187-excess
P90	10.9	1.4	WN8-9h	A2696	11.06	-0.025	-0.050	Table5
P91	11.0	2.5	WN5-6b	A5615	10.79	+0.129	-0.082	Table5
P96	11.0	2.0	WN9/Ofpe	A3755	10.95	+0.042	-0.117	Table5
P97	10.7	1.2		A4763	10.74	-0.109	-0.063	clear 187-excess
S61	11.5	1.0		A2779	11.49	-0.198	-0.071	small 187-excess
S62	13.3	1.0		A2954	13.45	-0.071	-0.028	small 187-excess
S133	11.7	1.0	O4-6I	A2756	11.76	-0.199	-0.051	no 187-excess
S135		1.0		A2804	11.55	-0.154	-0.019	no 187-excess

\*  $\log(n187) \equiv \log(F_{N1875}/F_{K_S}/0.0147)$  and  $\log(n207) \equiv \log(F_{N207}/F_{K_S}/0.130)$

We cannot identify 8 sources in Dong's list: P78, S6, S31, S59, S66, S132, S134, S137, (S3/4=P17?)

area is also consistent between Dong et al. (2011) and ours as described above.

### 4.3 A Relation between the Excess of $\log(n187)$ and Reddening-Free $K_S$ Magnitude in WN stars

In Fig. 4, we depict a relation between “reddening-free” or “extinction-corrected”  $K_S$  [mag] and “excess”  $\log(n187)$  for Arches data. Here

$$\text{reddening-free } K_S[\text{mag}] \equiv K_S[\text{mag}] + \log(n207) \times 32.6, \quad (5)$$

$$\text{excess } \log(n187) \equiv \log(n187) - \log(n207) \times 4.10. \quad (6)$$

Fig. 4 shows a clear correlation between them for WN stars. It is noted that the reddening-free  $K_S$  absolute magnitudes range from -7.5 to -4.5, which are consistent with  $M_{K_S}$  magnitudes for WN8-9 stars by Rosslowe & Crowther (2015).

The similar correlation has already reported by Figer et al. (2002). This correlation possibly means that when mass-loss rate increases,  $n187$ -excess due to He II line emission becomes larger and the  $K_S$  magnitude due to free-free radiation also becomes brighter. In this case, we may be able to estimate the inclination index of the above correlation as follows. The  $F_{N1875}$  excess flux originates in recombination lines of He II for WN stars, which have an dependence of  $\dot{M}^2$ .

On the other hand,  $K_S$  excess flux originates in free-free radiation, which has an dependence of  $\dot{M}^{4/3}$ . In consequence, we might expect an inclination index of -0.2 in the relation of Fig. 4. However, this value of the inclination is not accurate. In practice, the inclination derived from our data seems to be a little flatter than the “expected” value of -0.2. It is noted that one WN5-6b star (see Table 5) included in Fig. 4 does not affect this discussion. More detailed and accurate discussions of this correlation will be presented in the next paper (Osawa et al., in preparation).

It is known that the  $K_S$  magnitude of WN stars even with the same subtype distributes in several magnitudes (cf. Crowther 2007; Rosslowe & Crowther 2015). From the distribution of WN stars in Fig. 4, this dispersion is expected to be due to a variety of mass-loss rates. However, the reason why the same subtype of WN stars have a wide variety of mass-loss rates is not yet understood. On the other hand, a common “intrinsic”  $K_S$  absolute magnitude of  $\sim -4.5$  mag (excess  $\log(n187) = 0$ ) for WN8-9 stars can be found in Fig. 4. Here “intrinsic” means a  $K_S$  magnitude for a “bare” WN star without free-free emission.

The WN stars of the Galactic Center cluster area and the Quintuplet cluster area indicate similar relations, and WN9/Ofpe stars may have brighter “intrinsic”  $K_S$  magnitude than WN8-9 stars. Anyway, the Arches cluster which has many similar subtype stars (WN8-9) gives a good sample for considering the nature of WN stars.

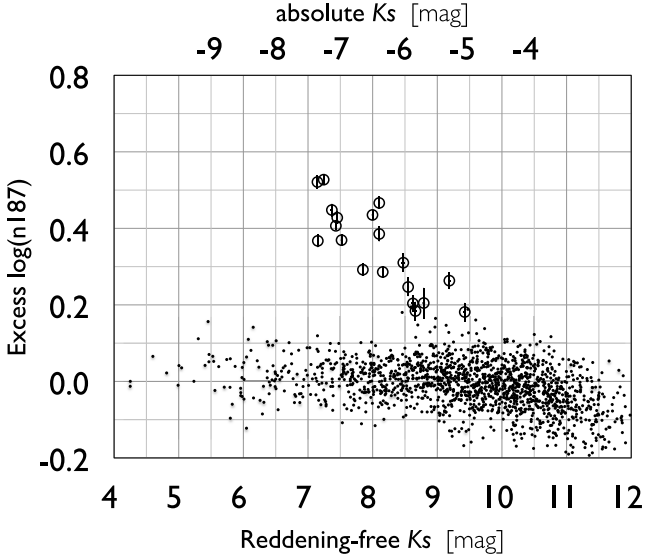


**Figure 4.** The relations between the reddening-free  $K_S$  magnitude and the excess of  $\log(n187)$  for the WN stars in the Arches cluster area. Open circles denote 19 WN stars (Table 5). Black dots denote residual 1602 stars; major of them with the reddening-free  $K_S > 8$  mag are possibly OB-type main-sequence or blue supergiants. On the other hand, the stars with the reddening-free  $K_S < 8$  mag can be red giants/supergiants or extremely red sources (Miras and non-Miras; see Section 4.5). It is noted that the  $K_S$  magnitude here for the extremely red sources is not real (see Section 4.5). The absolute  $K_S$  magnitude (the distance modulus of 14.5 magnitude is adopted) is indicated above the diagram.

#### 4.4 Distribution of Extinction $A_{K_S}$ from $\log(n207)$

By using the  $N207$  and  $K_S$  images, we can derive the extinction  $A_{K_S}$  (eq. (1)) for the sources with no specific emission in  $N207$ , with an assumption that stars have  $\lambda^{-4}$  spectra; this assumption is approximately satisfied for large variety of stars (see Sections 3.1 and 3.2). We derive the average extinction  $A_{K_S}$  of whole images to be 3.15, 2.40, and 2.43 mag for  $5' \times 5'$  area of the Galactic Center cluster, the Quintuplet cluster, and the Arches cluster, respectively (see Table 2). It is noted that the emission stars and extremely red sources (see Section 4.5) are excluded to derive the  $A_{K_S}$ . Moreover, we make a rough distribution of  $A_{K_S}$  in the images by dividing the  $5' \times 5'$  FOV into  $9 \times 9$  subareas as shown in Fig. 5 for the Galactic Center cluster area. Fig. 5 shows the average  $A_{K_S}$  in each  $30'' \times 30''$  with figures and grey gradation, and the  $A_{K_S}$  map is overlaid on the half-transparent  $K_S$  image. The  $30'' \times 30''$  squares without  $A_{K_S}$  figures have large errors in  $A_{K_S}$  due to small numbers of sources. For example, our extinction map shows  $A_{K_S}=2.73$  mag at the central  $30'' \times 30''$  area of the Galactic Center cluster area, and large extinction region with  $A_{K_S}$  of over  $\sim 4$  mag in the southeast area. Dong et al. (2011) also estimate the distribution of  $A_{K_S}$  ( $=0.76 A_{F190N}$ ) for their whole observed area, which shows it distributes 1 to 4 mag with peak=2.2 mag. On the other hand, our average  $A_{K_S}$  of the central  $40'' \times 40''$  of the Galactic Center cluster ( $=2.72$ ) is a little smaller than that by Schodel et al. (2010) ( $=3.04$ ), if extinction law of  $A_\lambda \propto \lambda^{-2.0}$  is adopted for their results. In the Quintuplet

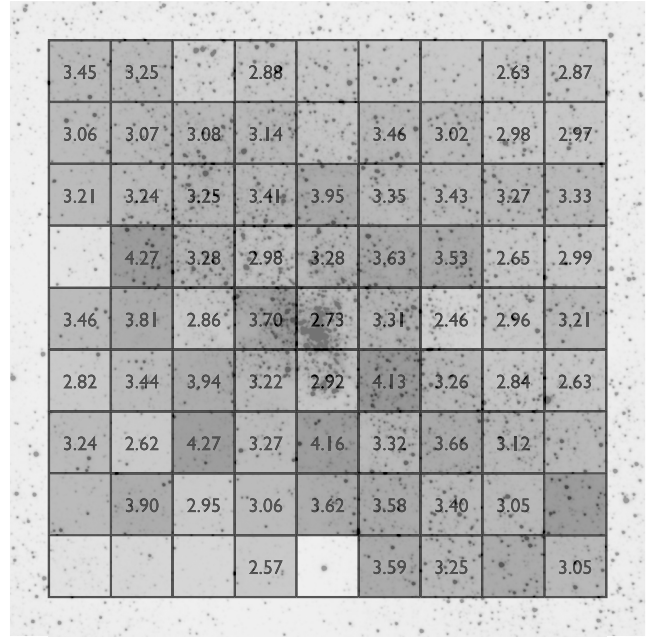


**Figure 5.** Distribution of  $A_{K_S}$  calculated from  $n207$  in the Galactic Center cluster area. A small box indicates  $30'' \times 30''$  area and the average  $A_{K_S}$  of the sources in the box is shown with figures and grey color corresponding to the  $A_{K_S}$ . Blank boxes (without  $A_{K_S}$  figures) show large errors in  $A_{K_S}$ . Typical errors of the  $A_{K_S}$  determination are 0.2-0.3 magnitude. The  $A_{K_S}$  map is overlaid on the  $K_S$  image.

and Arches areas,  $A_{K_S}$  seems to vary not so much in the  $5' \times 5'$  images.

#### 4.5 Extremely Red Sources with Apparent Large “ $A_{K_S}$ ”: Miras/LPVS and Candidates of Low-Temperature ( $T < 1000$ K) Sources

In Section 3.2, we derive  $A_{K_S}$  from  $F_{N207}/F_{K_S}$  for normal stars with approximately  $\lambda^{-4}$  spectra, but cannot derive  $A_{K_S}$  from  $F_{N207}/F_{K_S}$  for stars with non- $\lambda^{-4}$  spectra: i.e., emission-line stars like WC stars, and extremely red sources; ERS: Mira variables (Mira)/long-period variable stars (LPVS) and candidates of extremely low temperature sources. Here, in order to study the detected ERS, we use a kind of extinction map (Section 4.4) as the “local” interstellar extinction toward the sources.

Almost all WCLd and WC9 stars locate along the extinction-line with “ $A_{K_S}$ ” = 4-6 mag in our color-color diagrams. Here for these values of “ $A_{K_S}$ ” = 4-6 mag, we prefer to regard them not as real interstellar extinction but as a superposition of interstellar extinction  $A_{K_S} = 1-4$  mag and “additional”  $A_{K_S} \sim 3$  mag due to circumstellar extinction of the stars.

On the other hand, we also detected several tens of ERS which are nearly along the extinction-line with  $A_{K_S} > 6$  mag in our color-color diagram (Fig. 2). These sources can be divided into two groups: Miras/LPVSs and non-Miras. The Miras/LPVSs have the following characteristics compared with the non-Miras: 1) brighter, 2) spatially homogeneously distributed within our images. That is, the non-Miras are

**Table 9.** Extremely red sources: Miras and non-Miras

Area	Galactic Center	Quintuplet	Arches
total stars detected	3605	1955	1621
by us with $K_S < 13$ mag			
Mira detected <sup>1)</sup> (per total)	109 (3.0 %)	62 (3.2 %)	49 (3.0 %)
A case of “apparent” $A_{K_S}$ as real $A_{K_S}$			
Extremely-Red Mira <sup>1)</sup>	31	25	12
$A_{K_S}$ (ave) [mag]	$7.7 \pm 1.7$	$6.9 \pm 1.4$	$6.8 \pm 1.4$
dereddened $K_S$ (ave) [mag]	$2.8 \pm 1.5$	$3.1 \pm 1.7$	$3.7 \pm 1.8$
$M_{K_S}$ (ave) [mag]	$-11.7 \pm 1.5$	$-11.4 \pm 1.7$	$-10.8 \pm 1.8$
Extremely-Red non-Mira <sup>2)</sup>	41	15	9
$A_{K_S}$ (ave) [mag]	$7.0 \pm 0.7$	$6.0 \pm 0.9$	$5.5 \pm 0.4$
dereddened $K_S$ (ave) [mag]	$4.8 \pm 0.9$	$5.6 \pm 1.1$	$6.2 \pm 0.7$
$M_{K_S}$ (ave) [mag]	$-9.7 \pm 0.9$	$-8.9 \pm 1.1$	$-8.3 \pm 0.7$
A case of “local” $A_{K_S}$ as real $A_{K_S}$			
Extremely-Red Mira <sup>1)</sup>	31	25	12
$A_{K_S}$ (ave) [mag]	$3.2 \pm 0.6$	$2.2 \pm 0.4$	$2.5 \pm 0.7$
dereddened $K_S$ (ave) [mag]	$7.3 \pm 1.0$	$7.7 \pm 1.3$	$8.0 \pm 1.2$
$M_{K_S}$ (ave) [mag]	$-7.2 \pm 1.0$	$-6.8 \pm 1.3$	$-6.5 \pm 1.2$
Extremely-Red non-Mira <sup>2)</sup>	41	15	9
$A_{K_S}$ (ave) [mag]	$3.4 \pm 0.6$	$2.2 \pm 0.4$	$2.1 \pm 0.3$
dereddened $K_S$ (ave) [mag]	$8.5 \pm 1.0$	$9.4 \pm 1.0$	$9.7 \pm 0.6$
$M_{K_S}$ (ave) [mag]	$-6.0 \pm 1.0$	$-5.1 \pm 1.0$	$-4.8 \pm 0.6$

<sup>1)</sup> identified by Matsunaga et al. (2009)

<sup>2)</sup> sources with  $T < 1000$  K ; see text

less brighter than the Miras/LPVs and seem to be located in larger extinction regions.

First, we compared our ERS list with that of Miras/LPVs detected by Matsunaga et al. (2009). Matsunaga et al. (2009) have detected 1364 Miras/LPVs (including variable stars with less regularity and also three LBVs in the Quintuplet cluster area) in  $20' \times 30'$  area of the Galactic Center region and we identified almost all Miras/LPVs in their list located in our three  $5' \times 5'$  observed areas. The number of the identified sources are summarized in Table 9. According to this table, the ratios of the number of the detected Miras/LPVs (including Miras/LPVs which are not ERS) to the total number of our detections with  $K_S < 13$  mag are almost similar ( $\sim 3.0$  %) for three areas. If we adopt  $A_{K_S}$  directly derived from  $F_{N207}/F_{K_S}$  of themselves as their real interstellar  $A_{K_S}$ , the absolute  $K_S$  magnitudes of  $\sim -11$  are derived for the Miras/LPVs (upper part of Table 9). The  $M_{K_S}$  magnitudes of Miras/LPVs are reported to be  $-7 \pm 1$  by Matsunaga et al. (2009), therefore this value of  $\sim -11$  is much too bright! On the other hand, in the case that we adopt an average  $A_{K_S}$  derived from the neighbor normal stars (within  $10''$  from the ERS) as the “local” interstellar extinction for the ERS, the derived  $M_{K_S}$  magnitudes of Miras/LPVs agree well to them by Matsunaga et al. (2009) (lower part of Table 9). In practice, the spectra of Miras are much different from the  $\lambda^{-4}$  spectra (cf. Lancon & Wood 2000), and estimates of  $n_{207}$  and  $n_{187}$  of Miras based on the spectra (for example, R Cha by Lancon & Wood 2000) bring an “pseudo”  $A_{K_S}$  of  $\sim 3$  mag. The consideration here possibly makes the use of the “local”  $A_{K_S}$  as the real  $A_{K_S}$  for ERS reasonable.

Next, we discuss the residual ERS (non-Miras). In Ta-

bles 10-12 we list the residual ERS which are defined here to be “apparent”  $A_{K_S}$  larger than the “local” value plus 3 mag. In practice, these sources have “apparent”  $A_{K_S}$  much larger than 5 mag up to 10 mag. As described above, it is difficult to consider that the whole of “apparent”  $A_{K_S}$  up to 10 mag is real interstellar extinction. We had better consider that a part of large “apparent”  $A_{K_S}$  is contributed by much different spectra of the sources from  $\lambda^{-4}$ . As the candidates for the non-Mira group, very low temperature sources can be considered, such as low-mass evolved stars: OH/IR sources and/or red giants surrounded by thick dust envelopes, and massive young sources (MYSOs or UCHII regions). It is noted that most of these stars of the non-Mira group have no corresponding sources in SIMBAD. Some objects have IR or X-ray sources (comment of Tables 10-12) within  $2''$  from each source (our position accuracy is  $\sim 0''.5$ ). However, the relation between the non-Mira ERS and X-ray sources are unknown. On the other hand, most of the non-Mira ERS are detected with Spitzer/IRAC (cf. Ramírez et al. 2008) at least in one channel. The non-Miras ERS which are detected in 3 channels: [3.6], [4.5], and [8.0], are commented in Tables 10-12. They show [3.6]-[4.5] color of  $0.5 \sim 1.5$  mag, which are larger enough compared with the nominal interstellar extinction at the galactic center.

In order to consider a possibility of the low temperature sources as the candidates for the non-Mira group, we estimate the  $n_{207}$  and  $n_{187}$  values again for low-temperature sources. Considering simply, we calculate them for blackbody radiation. For example, the values for the blackbody with  $T=1000$ -600 K correspond to “pseudo”  $A_{K_S} = 2.8$ -5.6 mag almost along the extinction-line. In Fig. 6, we plot the relations between “reddening-free”  $\tilde{K}_S$  magnitude and

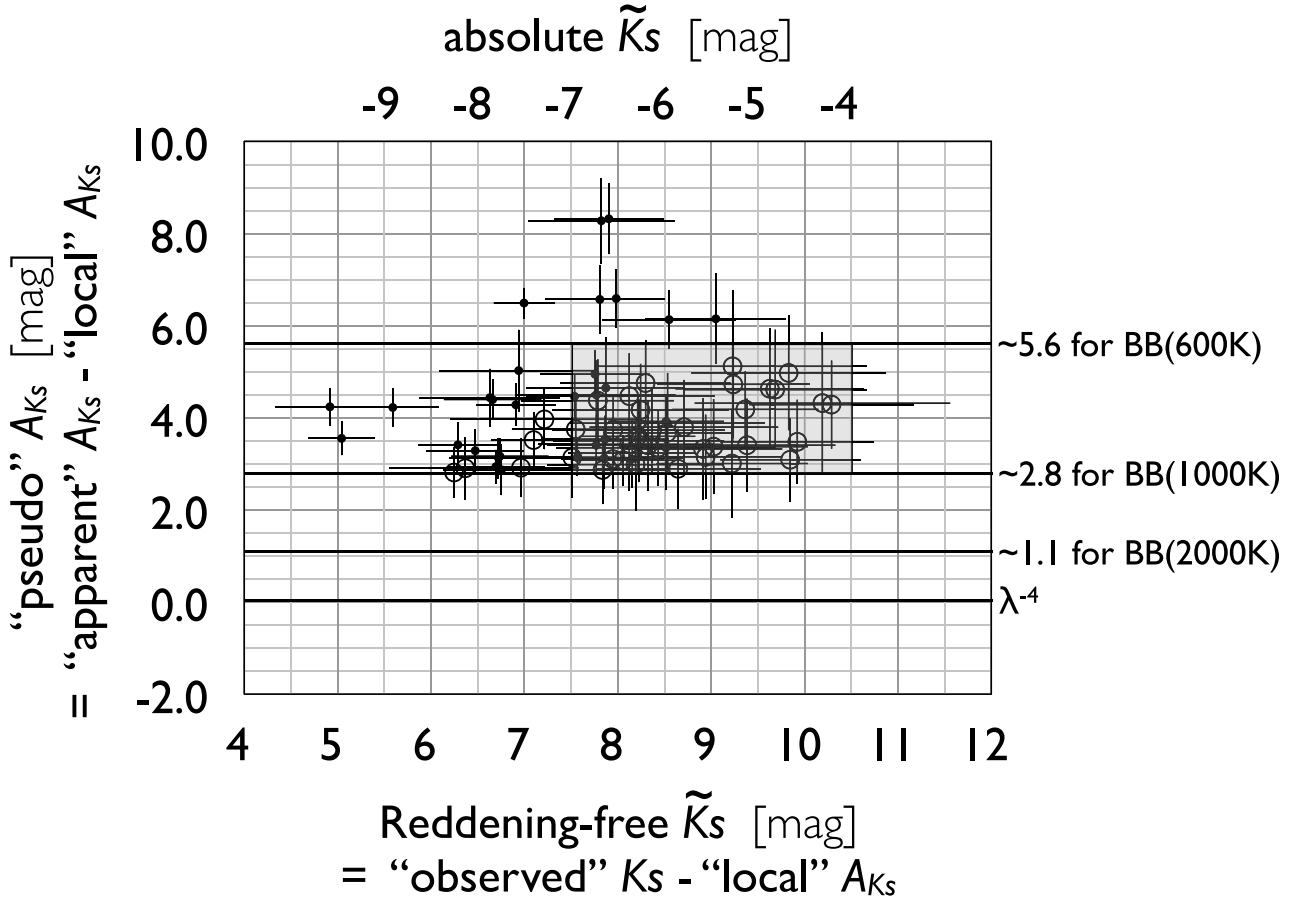


**Figure 6.** The relation between the “pseudo”  $A_{K_S}$  and the “reddening-free”  $\tilde{K}_S$  magnitude for the extremely red sources (ERS) in the Galactic Center cluster area. It is noted that the “reddening-free”  $\tilde{K}_S$  here is different from that of Fig. 4 (see text). The  $M_{K_S}$  magnitude are also shown above the diagram. Black dots and open circles denote Miras/LPVs and non-Miras of the ERS, respectively. Horizontal lines correspond to the values of “pseudo”  $A_{K_S}$  with blackbody (BB) temperatures (see text), and a gray box indicates typical areas for the observed ERS of non-Miras (see text).

“pseudo”  $A_{K_S}$  which are corrected with the “local” extinction  $A_{K_S}$  for the ERS in the Galactic Center cluster area. The “reddening-free”  $\tilde{K}_S$  magnitude here is different from that of section 4.3 (Fig. 4; equation (5)) and defined as

$$\text{reddening-free } \tilde{K}_S [\text{mag}] \equiv K_S [\text{mag}] - A_{K_S} (\text{local}). \quad (7)$$

Fig. 6 shows that the Miras/LPVs are distributed in the range of “reddening-free”  $\tilde{K}_S [\text{mag}] = 5.5 \sim 8.5$ , which corresponds to  $M_{K_S}$  magnitude of  $-9 \sim -6$  (cf. Matsunaga et al. 2009, see above). Furthermore, in spite of the Miras/LPVs and the non-Miras have similar “pseudo”  $A_{K_S}$ , the non-Miras have larger  $\tilde{K}_S$  magnitude of  $7.5 \sim 10.5$  mag, corresponding to  $M_{K_S}$  magnitude of  $-7 \sim -4$ , which are fainter than those of the Miras/LPVs by an order of magnitude. This  $M_{K_S}$  magnitude may be similar to a typical value of massive young stars. For example,  $M_{K_S}$  magnitude of W51 IRS2W and IRS2E (these sources are possibly multiplets) is estimated to be  $-6.6$  and  $-6.4$ , respectively, with an assumption of the distance of 5 kpc (Okumura et al. 2000). It is noted that M-type giants has usually  $M_{K_S} > -4$  mag, then the majority of the non-Mira ERSs are probably not M giants. In these wavelengths, although it may be difficult to detect MYSO in the earliest stage of evolution, we expect to detect a little evolved sources with thick dust en-

velopes such that UCH II region, for example. Anyway, future detailed observations are desired. The other areas show a similar situation, although the sample is small.

## 5 SUMMARY

The University of Tokyo constructed a 1-m infrared telescope (miniTAO) at extremely high altitude site of 5640 m; the summit of Cerro Chajnantor, Atacama, northern Chile, in 2009. In the same site, a 6.5-m infrared telescope (TAO) are now going to be constructed. From this site, we can make seamless observations in near-infrared wavelengths. In particular, the wavelength range of  $1.87 \mu\text{m}$  opens to us, so that strong Pa $\alpha$  emission can be observed from the ground. By using this miniTAO with such a superior condition, we carried out near-infrared narrow-band imaging observations of three galactic center clusters: the Galactic Center cluster, the Quintuplet cluster, and the Arches cluster in  $1.87 \mu\text{m}$ ,  $2.07 \mu\text{m}$ , together with  $K_S$ .

Color-color diagrams made from the images clearly show excess of  $1.87 \mu\text{m}$  due to He II and/or Pa $\alpha$  emission for WN stars and LBVs, and excess of  $2.07 \mu\text{m}$  due to C IV emission for WC stars. Almost all known WRs and LBVs in our observed areas are detected except for in the very

**Table 10.** Extremely red sources (non-Miras) in the Galactic Center cluster area

ID	RA(2000)	DEC(2000)	$K_S$ [mag]	$\log(n187)^{1)}$	$\log(n207)^{1)}$	“apparent” $A_{K_S}^{2)}$	“local” $A_{K_S}$	comment $^{3)}$
C2649	17:45:41.28	-29:00:49.9	10.10	-0.773	-0.210	6.86	2.89	BSD96-110
C659	17:45:46.10	-29:02:17.2	10.25	-0.900	-0.209	6.81	4.00	SSTGC
C4963	17:45:42.06	-28:59:34.6	10.43	-0.647	-0.186	6.05	2.92	
C2061	17:45:39.96	-29:01:11.0	10.47	-0.853	-0.215	7.01	4.10	BSD96-180
C3895	17:45:44.77	-29:00:08.4	10.90	-0.881	-0.218	7.10	3.35	BSD96-214
C1973	17:45:35.89	-29:01:13.8	10.97	-0.696	-0.184	6.00	2.92	
C5060	17:45:39.29	-28:59:30.2	11.01	-0.783	-0.228	7.43	3.91	
C1734	17:45:38.97	-29:01:23.9	11.17	-0.772	-0.218	7.12	4.20	CXOGC
C5422	17:45:38.18	-28:59:17.6	11.24	-0.748	-0.196	6.40	3.30	CXOGC
C6219	17:45:48.38	-28:58:52.9	11.34	-0.745	-0.197	6.42	3.19	SSTGC
C1307	17:45:41.04	-29:01:44.8	11.50	-0.672	-0.208	6.77	3.27	
C3319	17:45:45.41	-29:00:27.6	11.63	-0.815	-0.208	6.78	3.10	SSTGC
C7305	17:45:34.98	-28:58:07.4	11.68	-0.854	-0.199	6.50	2.31	
C1225	17:45:43.37	-29:01:49.3	11.74	-0.812	-0.219	7.13	3.53	SSTGC
C1916	17:45:47.06	-29:01:18.4	11.76	-1.062	-0.205	6.68	3.32	SSTGC
C1843	17:45:40.07	-29:01:19.4	11.78	-0.732	-0.202	6.57	3.59	
C1239	17:45:43.95	-29:01:48.7	11.80	-0.955	-0.253	8.26	3.50	SSTGC
C4703	17:45:47.67	-28:59:42.9	11.83	-0.961	-0.258	8.42	4.04	
C3185	17:45:48.75	-29:00:33.1	11.85	-0.941	-0.234	7.64	3.90	SSTGC
C1420	17:45:44.92	-29:01:39.6	11.85	-0.868	-0.252	8.20	3.73	
C1812	17:45:39.51	-29:01:20.8	11.90	-0.849	-0.212	6.93	4.06	
C4149	17:45:49.14	-29:00:01.5	12.05	-0.729	-0.185	6.05	1.76	
C2468	17:45:40.66	-29:00:56.0	12.07	-0.785	-0.235	7.56	2.84	SSTGC $^{4)}$
C5856	17:45:48.80	-28:59:05.0	12.08	-0.824	-0.220	7.16	3.76	
C899	17:45:36.38	-29:02:03.0	12.11	-0.656	-0.194	6.33	3.17	CXOGC
C3072	17:45:48.17	-29:00:36.8	12.15	-0.912	-0.229	7.45	4.03	
C1559	17:45:45.24	-29:01:33.4	12.19	-1.004	-0.249	8.11	3.94	
C2555	17:45:48.34	-29:00:54.7	12.23	-0.784	-0.199	6.48	3.59	
C1950	17:45:44.34	-29:01:16.2	12.32	-0.731	-0.236	7.69	3.96	
C422	17:45:38.86	-29:02:28.7	12.33	-0.851	-0.180	5.88	2.40	
C4009	17:45:35.65	-29:00:02.5	12.34	-0.699	-0.171	5.58	2.49	
C2196	17:45:49.97	-29:01:08.6	12.35	-0.967	-0.205	6.70	3.32	
C5505	17:45:47.86	-28:59:16.6	12.41	-0.760	-0.197	6.43	3.02	
C1633	17:45:37.45	-29:01:28.2	12.41	-0.943	-0.227	7.41	2.78	
C866	17:45:46.77	-29:02:07.1	12.49	-0.897	-0.233	7.58	3.79	CXOGC
C1834	17:45:47.65	-29:01:21.5	12.52	-0.872	-0.212	6.93	3.60	SSTGC
C1123	17:45:44.17	-29:01:54.1	12.60	-0.736	-0.196	6.39	3.38	SSTGC
C3481	17:45:49.90	-29:00:22.9	12.72	-1.026	-0.241	7.86	2.89	
C6103	17:45:47.19	-28:58:56.5	12.90	-1.003	-0.270	8.79	3.67	
C3697	17:45:48.82	-29:00:15.9	12.97	-0.829	-0.218	7.10	2.78	
C1142	17:45:44.26	-29:01:53.4	13.00	-1.089	-0.243	7.92	3.31	

sources with  $T < 1000$  K ; see text

$^{1)}$   $\log(n187) \equiv \log(F_{N1875}/F_{K_S}/0.0161)$ ,  $\log(n207) \equiv \log(F_{N207}/F_{K_S}/0.130)$

$^{2)}$  “apparent”  $A_{K_S} = -32.6 \times \log(n207)$

$^{3)}$  sources within  $2''$  from the objects in SIMBAD; BSD96 by Blum et al. (2003); CXOGC by Muno et al. (2009)

sources as SSTGC here are detected within  $1''$  in 3 channels ([3.6], [4.5], [8.0]) of Spitzer/IRAC, see text.

$^{4)}$  this source is also identified as V4513 Sgr (OH/IR), BSD96-188

near the Galactic Center. Our detections in the  $1.87 \mu\text{m}$  images agree well with *Hubble Space Telescope* observations by Dong et al. (2011). Moreover, WN stars show a clear relation between the 187-excess and reddening-free  $K_S$  magnitude. In this relation we found a common  $M_{K_S}$  magnitude of  $\sim -4.5$  for WN stars in the Arches cluster.

The extinction for each star is also derived from the color-color diagrams, and extinction maps of the areas can be made. Furthermore, almost all Mira variables reported by Matsunaga et al. (2009) are detected. By using the local extinction maps, several tens of the extremely red sources

(ERS) except for Miras are also detected. They are possibly considered to be low-temperature (600-1000 K) sources.

In practice,  $1.87 \mu\text{m}$  observations are possible only at miniTAO telescope (in the near future, at TAO) from the ground, and the combination of  $1.87 \mu\text{m}$ ,  $2.07 \mu\text{m}$ , and  $K_S$  images are strong tools to search massive stars in various types, especially in large extinction regions. We have carried out the similar observations in the Westerlund 1 cluster and in LMC and successive papers are being prepared.

**Table 11.** Extremely red sources (non-Miras) in the Quintuplet cluster area

ID	RA(2000)	DEC(2000)	$K_S$ [mag]	$\log(n187)^{1)}$	$\log(n207)^{1)}$	“apparent” $A_{K_S}^{2)}$	“local” $A_{K_S}$	comment <sup>3)</sup>
Q129	17:46:14.39	-28:52:05.0	9.49	-0.687	-0.76	5.75	2.84	SSTGC
Q1170	17:46:10.38	-28:51:19.9	10.90	-0.667	-0.158	5.15	2.08	
Q702	17:46:02.66	-28:51:39.3	11.04	-0.721	-0.170	5.53	2.43	SSTGC
Q377	17:46:21.77	-28:51:56.4	11.05	-0.810	-0.199	6.49	1.79	
Q949	17:46:15.93	-28:51:30.6	11.24	-0.600	-0.162	5.28	2.26	
Q3955	17:46:16.52	-28:49:24.4	11.37	-0.561	-0.170	5.53	2.28	LHO136 (M2I)
Q1256	17:46:18.20	-28:51:17.4	11.49	-0.607	-0.155	5.04	2.07	SSTGC
Q5690	17:46:03.68	-28:47:58.9	11.59	-0.683	-0.175	5.69	1.96	
Q1568	17:46:10.72	-28:51:03.5	11.84	-0.742	-0.204	6.66	1.70	SSTGC
Q5950	17:46:09.64	-28:47:47.1	11.85	-0.682	-0.169	5.52	2.21	
Q5430	17:46:10.68	-28:48:13.9	11.90	-0.852	-0.257	8.37	2.64	
Q2010	17:46:19.59	-28:50:46.1	12.25	-0.807	-0.219	7.12	2.15	
Q1008	17:46:12.71	-28:51:27.2	12.29	-0.937	-0.195	6.37	1.67	SSTGC
Q1097	17:46:12.43	-28:51:22.8	12.65	-0.574	-0.167	5.44	1.86	
Q1359	17:46:21.92	-28:51:13.4	12.89	-0.641	-0.178	5.81	2.62	SSTGC

sources with  $T < 1000$  K ; see text

<sup>1)</sup>  $\log(n187) \equiv \log(F_{N1875}/F_{K_S}/0.0134)$ ,  $\log(n207) \equiv \log(F_{N207}/F_{K_S}/0.130)$

<sup>2)</sup> “apparent”  $A_{K_S} = -32.6 \times \log(n207)$

<sup>3)</sup> sources within 2'' from the objects in SIMBAD; LHO by Liermann et al. (2009)

sources as SSTGC here are detected within 1'' in 3 channels ([3.6], [4.5], [8.0]) of Spitzer/IRAC, see text.

**Table 12.** Extremely red sources (non-Miras) in the Arches cluster area

ID	RA(2000)	DEC(2000)	$K_S$ [mag]	$\log(n187)^{1)}$	$\log(n207)^{1)}$	“apparent” $A_{K_S}^{2)}$	“local” $A_{K_S}$	comment <sup>3)</sup>
A311	17:45:42.73	-28:47:35.9	10.60	-0.659	-0.155	5.05	1.80	SSTGC
A291	17:45:48.09	-28:47:36.5	11.11	-0.695	-0.166	5.41	1.93	SSTGC
A6648	17:45:44.59	-28:52:03.4	11.20	-0.584	-0.158	5.15	1.63	
A1201	17:45:52.72	-28:48:17.9	11.77	-0.639	-0.194	6.33	2.52	
A6515	17:45:56.16	-28:52:01.2	11.79	-0.678	-0.177	5.79	2.52	
A2397	17:45:51.02	-28:49:07.8	12.08	-0.698	-0.179	5.85	2.21	
A5206	17:45:52.50	-28:51:08.2	12.16	-0.632	-0.177	5.78	1.96	
A1673	17:45:57.98	-28:48:39.7	12.28	-0.701	-0.156	5.09	2.16	
A443	17:45:51.86	-28:47:44.8	12.65	-0.597	-0.157	5.11	2.06	

sources with  $T < 1000$  K ; see text

<sup>1)</sup>  $\log(n187) \equiv \log(F_{N1875}/F_{K_S}/0.0147)$ ,  $\log(n207) \equiv \log(F_{N207}/F_{K_S}/0.130)$

<sup>2)</sup> “apparent”  $A_{K_S} = -32.6 \times \log(n207)$

<sup>3)</sup> sources as SSTGC here are detected within 1'' in 3 channels ([3.6], [4.5], [8.0]) of Spitzer/IRAC, see text.

## ACKNOWLEDGMENTS

We thank Drs. N. Matsunaga, and S. Nishiyama for some helpful suggestions and discussion. This research has been supported in part by the Ministry of Education, Culture, Sports, Science and Technology of Japan, Grand-in-Aid for Scientific Research (22253002, 22540258, 23540259, 25400226) from the JSPS. Operation of ANIR on the mini-TAO 1-m telescope is supported by NAOJ Research Grant for Universities and Optical/Near-Infrared Astronomy Inter-University Cooperation Program and Optical/Infrared Synergetic Telescopes of Education/Research.

## REFERENCES

- Blum R.D., Ramirez S.V., Sellgren K., Olsen K., 2003, ApJ, 597, 323  
 Conti P. S., 1975, Memoires of the Societe Royale des Sciences de Liege, 9, 193  
 Crowther P.A., 2015, Proceedings of “Walf-Rayet Stars” eds. by Hamann W.-R., Sander A., and Todt H., 21  
 Crowther P.A., 2007, ARA&A, 45, 177  
 Davies B., de la Fuente D., Najarro, F., Hinton J.A., Trombley C., Figer D.F., Puga E., 2012, MNRAS, 419, 1860  
 Dong H., Wang Q.D., Cotesa A., Stolovy S., Morris M.R., Mauerhan J., Mills E.A., Schneider G., Calzetti D., Lang C., 2011, MNRAS, 417, 114  
 Eisenhauer F., Genzel R., Alexander T., 2005, ApJ, 628, 246

- Figer D. F., et al., 2002, *ApJ*, 581, 258
- Figer D. F., McLean I. S., Morris M., 1999, *ApJ*, 514, 202
- Homeier N.L., Blum R.D., Pasquali A., Conti P.S., Damineli A., 2003, *A&A*, 408, 153
- Homeier N.L., Blum R.D., Conti P.S., Damineli A., 2003, *A&A*, 397, 585
- Konishi M., et al., 2015, *PASJ*, 67, 4
- Lancon A., Wood P.R., 2000, *A&A*, 146, 217
- Liermann A., Hamann W.-R., Oskinova L.M., 2009, *A&A*, 494, 1137
- Martins F., Hillier D.J., Paumard T., Eisenhauer F., Ott T., Genzel R., 2008, *A&A*, 478, 219
- Martins F., Genzel R., Hillier D.J., Eisenhauer F., Paumard T., Gillessen S., Ott T., Trippe S., 2007, *A&A*, 468, 233
- Matsunaga N., Kawazu T., Nishiyama S., Nagayama T., Hatano H., Tamura M., Glass I.S., Nagata T., 2009, *MNRAS*, 399, 1709
- Mauerhan J.C., Van Dyk S.D., Morris P.W., 2011, *AJ*, 142, 40
- Mauerhan J.C., Muno M.J., Morris M.R., Stolovy S.R., Cotera A., 2010a, *ApJ*, 710, 706
- Mauerhan J.C., Morris M.R., Cotera A., Dong H., Wang Q.D., Stolovy S.R., Lang C., Glass I.S., 2010b, *ApJ*, 713, L33
- Mauerhan J.C., Cotera A., Dong H., Morris M.R., Wang Q.D., Stolovy S.R., Lang C., 2010c, *ApJ*, 725, 188
- Minezaki T., et al., 2010, *Proc. SPIE*, 7733, 773356
- Motohara K., et al., 2008, *Proc. SPIE*, 7014, 70142
- Muno M.P., et al., 2009, *ApJS*, 181, 110
- Nishimaki Y., Yamamuro T., Motohara K., Miyata T., Tanaka M., 2008, *PASJ*, 60, 191
- Nishiyama S., Nagata T., Tamura M., Kandori R., Hatano H., Sato S., Sugitani K., 2008, *ApJ*, 680, 1174
- Nishiyama S., Nagata T., Kusakabe N., Matsunaga N., Naoi T., Kato D., Nagashima C., Sugitani K., Tamura M., Tanabe T., Sato S., 2006, *ApJ*, 638, 839
- Okumura S., Mori A., Nishihara E., Watanabe E., Yamashita T., 2000, *ApJ*, 543, 799
- Rosslowe C.K., Crowther P.A., 2015, *MNRAS*, 447, 2322
- Ramírez S.V., Arendt R.G., Sellgren K., Storovy S.R., Cotera A., Smith H.A., Yusef-Zadeh F., 2008, *ApJS*, 175, 147
- Schodel R., Najarro F., Muzic K., Eckart A., 2010, *A&A*, 511, A18
- Schodel R., Eckart A., Alexander T., 2007, *A&A*, 469, 125
- Shara M.M., et al., 2012, *AJ*, 143, 149
- Shara M.M., et al., 2009, *AJ*, 138, 402
- Smartt S.J., 2009, *ARA&A*, 47, 63
- Tanabé T., Motohara K., Tateuchi K., Matsunaga N., Ita Y., Toshikawa K., Kobishi M., Kato N., Yoshii Y., 2013, *PASJ*, 65, 55
- Tateuchi K., et al., 2015, *ApJS*, 217, 1
- Tateuchi K., et al., 2012, *Proc. SPIE*, 8446, 84467
- van der Hucht K.A., 2006, *A&A*, 458, 453
- van der Hucht K.A., 2001, *New Astronomy Reviews*, 45, 135
- Yamamuro T., Nishimaki Y., Motohara K., Miyata T., Tanaka M., 2007, *PASJ*, 59, 973
- Zwart S.F.P., McMillan S.L.W., Gieles M., 2010, *ARA&A*, 48, 431